

# Morphing Hydrofoil Model Driven by Compliant Composite Structure and Cavity Pressure

Fatiha Mohammed Arab<sup>1</sup>, Benoit Augier<sup>2</sup>

François Deniset<sup>1</sup>, Pascal Casari<sup>3</sup>, Jacques, Andre Astolfi<sup>1</sup>

<sup>1</sup>French Naval Academy Research Institute IRENav EA3634, Brest, France

<sup>2</sup>IFREMER, Brest, France

<sup>3</sup>Research Institute in Civil Engineering and Mechanics GeM, Saint-Nazaire, France

## ABSTRACT

In this work a collaborative experimental study is conducted in order to assess the effect on the hydrodynamic performance of a compliant composite hydrofoil controlled by an imposed cavity pressure. It is expected that the cavity pressure together with composite structures is suitable to control the hydrodynamic forces as well as cavitation inception and development. A new concept of morphing hydrofoil is developed by the authors and tested in the cavitation tunnel at the French Naval Academy Research Institute. The experiments are based on the measurements of hydrodynamic forces and hydrofoil deformations under various conditions of cavity pressure. Effect on cavitation inception are shortly studied too. In parallel to this experiment, a 2D numerical tool is developed in order to help to design a compliant hydrofoil shape. Numerically, the fluid structure coupling is based on an iterative method under small perturbation hypothesis. The flow model is based on a panel method and a boundary layer formulation and it is coupled with a finite-element method for the structure. It is shown that pressure driven compliant composite structure is suitable to some extent to control the hydrodynamics forces allowing to enlarge the operational domain of the compliant hydrofoil according to the angle of attack and the cavity pressure. Preliminary results on cavitation inception driven by compliant composite wall are pointed out as well.

## Keywords

smart-structure, hydrofoil, morphing, compliant, composite, cavitation.

## 1 NOMENCLATURE

<i>CSD</i>	Computational Structural Dynamics
<i>FSI</i>	Fluid Structure Interaction
$\alpha$ , AoA	angle of attack [°]
$\epsilon$	convergence criteria
$\rho$	fluid density [kg/m <sup>3</sup> ]
$\sigma$	cavitation number: $\sigma = \frac{P - P_v}{\frac{1}{2}\rho V^2}$
$c$	hydrofoil chord [m]

$C_D$	drag coefficient: $C_D = \frac{D}{\frac{1}{2}\rho V^2 s}$
$C_L$	lift coefficient: $C_L = \frac{L}{\frac{1}{2}\rho V^2 s}$
$D$	drag force [N]
$\Delta P = P_{atm} - P_{cavity}$	internal cavity pressure [bar]
$e$	hydrofoil span [m]
$L$	lift force [N]
$P$	pressure [bar]
$q$	dynamic pressure : $q = \frac{1}{2}\rho V^2$
$Re$	Reynolds number: $Re = Vc/\nu$
$s$	hydrofoil planform
$U$	total displacement [m]
$V$	inflow velocity [m/s]
$X, Y, Z$	foil coordinates [m]
$\nu$	kinematic viscosity [m <sup>2</sup> /s]

## 2 INTRODUCTION

In naval applications, it is crucial to make strategic decision to reduce the fuel oil consumption of ships and therefore to decrease their CO<sub>2</sub> emissions. The demand of the reduction of fuel oil consumption and CO<sub>2</sub> emission is greater than ever before (Coraddu & al 2018). Underlying the need for improved performance, better comfort and stability, use of new concepts of innovative hydrofoils or propeller blades can be an option to improve the hydrodynamic performance and consumption of a ship. Using this new concept should permit to control the lift (thrust) and to reduce the drag for various operating conditions. However this can lead to cavitation onset at high speed and moderate angles of incidence but also at low speed and high angles. Improving the hydrodynamic performances and delaying the cavitation inception requires the modification of shape, hence the idea of using morphing hydrofoils. Currently, hydrofoils use mechanical systems as flap to modify their shape and to control their performance. Morphing structures could be an interesting path to change the performance (Weisshaar 2013).

In aerodynamic application, the use of morphing structures has proved its effect (Dimino and al 2017). Brailovski & al (2008) have numerically studied the effect on the aerodynamic performance and foil mechanical properties of a flexible suction side powered by two actuators.

Fluid Structure Interaction was investigated experimentally by studying the structural response of a flexible lightweight hydrofoil undergoing various flow conditions including cavitating flow by Lelong & al (2018). An optimization of the design of the shape and the elastic characteristics of a hydrofoil equipped with deformable elements providing flexibility to the trailing edge was developed by Sacher and al (2018). In their study, Zarruk & al (2014) investigated experimentally the effect of material and Reynolds number on the hydrodynamic performance of hydrofoils. They studied the performances of flexible hydrofoils of similar geometry made of stainless steel, aluminum and composite of carbon-fiber reinforced plastic with layups orientations at  $0^\circ$  and  $30^\circ$ . They concluded that the composite hydrofoils have the best hydrodynamic performance. Showing the potential of hydroelastic tailored composite hydrofoil.

The bend-twist coupling effects on the hydroelastic response of composite hydrofoils are experimentally studied by Young & al (2018). They concluded that bend-twist coupling affects the deformation of the hydrofoils which affected the hydrodynamic performance. In order to assess the effect of the cavitation on the structural response, Ducoin & al (2012) have studied the displacement of a flexible hydrofoil in a cavitating flow. They found that the hydrodynamic loading unsteadiness increases the vibrations experienced by the hydrofoil. Numerically, Garg, Lyu and al (2015) have developed a shape optimization tool to predict the hydrodynamic performance including the cavitation inception conditions.

In order to control the lift generated by hydrofoils on boats, Giovannetti & al (2018) have numerically and experimentally evaluated hydrofoil geometry designed to reduce passively the lift coefficient by increasing the flow velocity. This study was achieved through the use of wind tunnel experiments including deformation measurements where a good agreement was found with the numerical results. They found that the twist deformations resulted in a reduction in the effective angle of attack by 30% at higher flow velocities, which significantly reduced the foil lift and drag.

The French Naval Academy Research Institute (IRENav), the Research Institute in Civil Engineering and Mechanics and Ifremer have initiated a research program related to compliant hydrofoils for naval applications. The objective is to characterize a compliant composite hydrofoil driven by a cavity low pressure regarding the lift and drag forces as well as cavitation inception. This paper presents the experimental study performed in the hydrodynamic tunnel at the Research Institute of French Naval Academy. The hydrofoil manufactured at Research Institute in Civil Engineering and Mechanics (Saint-Nazaire) is firstly tested in open air to assess the effect of the cavity pressure on hydrofoil deformations by the use of digital image correlation (DIC-3D) system. Then, the hydrofoil is tested in the cavi-

tion tunnel at IRENav where the lift coefficient and the hydrofoil deformations are measured. In accordance with the experiments, a numerical approach based on a fluid structure coupling algorithm is developed. The paper describes the experimental setup, the numerical FSI algorithm and presents the main results.

### 3 EXPERIMENTAL SETUP

The experiments are carried out in the cavitation tunnel at IRENav (figure 1). The test section is 1 m length with a square section of 0.192 m side. The inflow velocity ranges between 0.5 and 12 m/s and the pressure in the tunnel test section ranges between 100 mbar to 3 bar to control the cavitation.



**Figure 1:** Hydrodynamic tunnel test section at IRENav with the compliant composite hydrofoil.

The compliant composite hydrofoil was manufactured at the Research Institute in Civil Engineering and Mechanics (GeM) (Figure 2). At rest, the compliant composite hydrofoil has a NACA 0012 section and a rectangular plan-form of 0.191 m span and 0.15 m chord length. It is cantilevered and clamped on a cylindrical aluminium beam fitted the hydrodynamic balance. The axis of rotation is at  $X/c = 0.25$ .

The hydrofoil is composed of a compliant wall, a rigid part and a pressurized cavity bounded by the compliant wall and controlled by a pneumatic actuator. The geometry of the hydrofoil can be modified by varying the cavity pressure. The following part, pressure will always correspond to a suction inside the hydrofoil compared to atmospheric reference. It is defined as  $\Delta P$  (called pressure cavity in the paper) has a positive value as it decreases. Figure 3 illustrates the pressure system, the compliant composite hydrofoil and the pneumatic actuator. The pressure into the cavity is measured using a manometer.

The compliant wall is laminate composed of three carbon/epoxy plies oriented at  $0^\circ/90^\circ$ . The laminate is thinner at the leading and trailing edge. These two parts are composed of two plies: one of carbon/epoxy [ $0^\circ/90^\circ$ ] and the second of glass fiber with orientation at  $45^\circ$ . The rigid side is composed of five plies of carbon/epoxy with the layups orientations at  $0^\circ$  and  $90^\circ$ .

To assess the effect of the cavity pressure on hydrofoil deformations in open air, the chordwise displacement of skin is investigated using the digital image correlation (DIC-3D) system at GeM laboratory (figure 4). This method is based on optimal strain measurements. It is non-contact processes and is particularly suitable for flexible materials. It is based on the comparison of two digital images features of the composite surface before and after deformation; total strain data can be obtained. For this purpose a two-camera system has been used to monitor the strain pre-gressing on the surface. In order to produce fine and exploitable details, a random pattern of paint is usually applied to the surface of the hydrofoil (De Barros & al, 2018) (figure 5).

The hydrofoil displacement is also investigated in open air by using a micrometric touch probe at a discrete position ( $Z/c = 0.33$ ,  $X/c = 0.63$ ) for various imposed cavity pressure of  $\Delta P = 0.15 \text{ bar}$ ,  $0.4 \text{ bar}$  and  $0.51 \text{ bar}$ .

In the hydrodynamic tunnel, the static deformation is measured using a Laser distance measurement system mounted on a 2D translation system on the upper side of the test section. The system allows us to scan the hydrofoil surface for a given flow condition along various sections selected along the span. In that case nine sections from the root to the tip are selected. Then the deformation is obtained by comparing the scans between the tested cavity pressures.

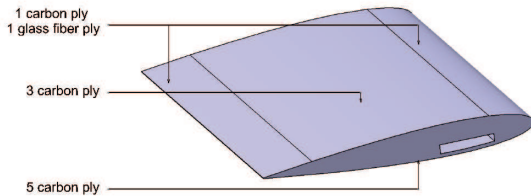


**Figure 2:** Laminate structure of the compliant composite hydrofoil.



**Figure 3:** Compliant hydrofoil to be deformed by control of the cavity pressure with a pneumatic actuator.

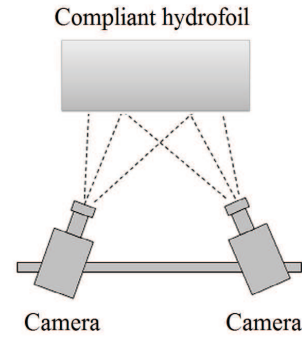


**Figure 4:** Digital image correlation (DIC) schematic at GeM (Saint-Nazaire, France).

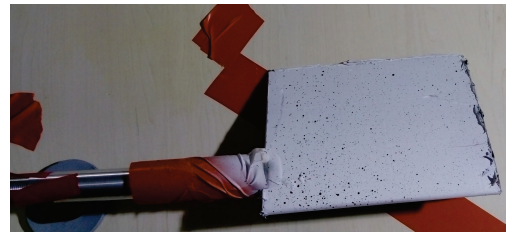


**Figure 5:** Specimen prepared for DIC with random pattern paint on the surface.

In the hydrodynamic tunnel, measurement of hydrodynamic forces are performed using a hydrodynamic balance at various conditions of cavity pressure and angle of attack at a flow velocity of  $5 \text{ m/s}$  corresponding to a Reynolds number of  $0.75 \cdot 10^6$ . The 5-component hydrodynamic balance has a range up to  $1700 \text{ N}$  for the lift force,  $180 \text{ N}$  for the drag and a  $43 \text{ Nm}$  for the pitching moment. It is fixed into a supporting frame, mounted on bearings, and driven in rotation by a Baldor motor. The stepper motor allows for 600 000 impulsions per rotation, meaning a resolution of  $6 \cdot 10^{-4}^\circ$ . The foil is fastened into the balance, secured by a tight fitted key/nut system (Marchand, Astolfi & Bot, 2017).

#### 4 NUMERICAL APPROACH

The numerical study consists of 2D simulation to investigate the effect of a static cavity pressure on the structural response of the compliant hydrofoil as well as the impact on hydrodynamic performances.

The flow model of the XFOIL solver and the finite-element method of the ANSYS-Mechanical solver are used for the FSI analysis. The FSI algorithm is based on an iterative method between the two solvers under small perturbation hypothesis. The flow model is based on the coupling between a panel method with a boundary layer model. The panel method accelerates the flow calculations as compared to finite volume methods. The coupling algorithm is developed using Python-scripts. The fluid structure coupling algorithm is described in figure 6. The FSI algorithm is initialized by a structural computation as the hydrofoil is submitted only to a cavity pressure. It leads to displace-

ments which conduct to a new hydrofoil shape. Then, the viscous flow around the new foil is solved. The external hydrodynamic pressure resulting from the  $C_p$  distribution is applied during the structural resolution. The problem is solved using an iterative method until the convergence on the maximum structural displacement and the lift coefficient  $C_L$  is reached. The convergence to the equilibrium of the hydrofoil is obtained after a small number of iterations showing that the method developed in this work has an advantage compared to advanced CFD-CSD solvers that require very important CPU times.

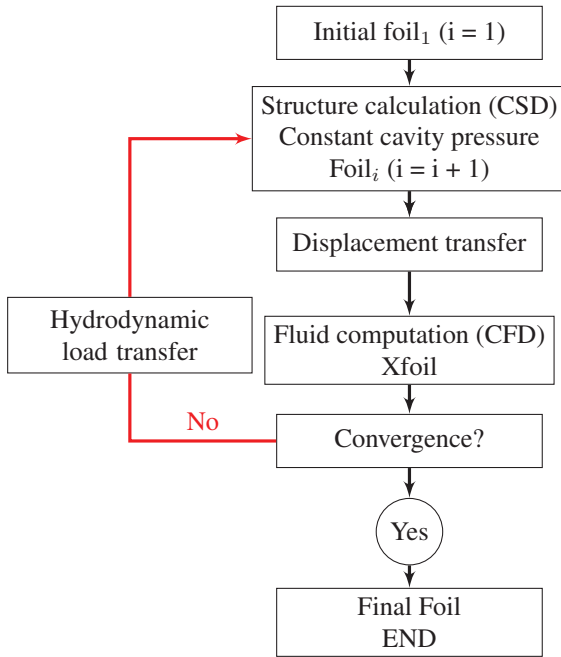


**Figure 6:** Schematic algorithm of fluid structure coupling with imposed cavity pressure.

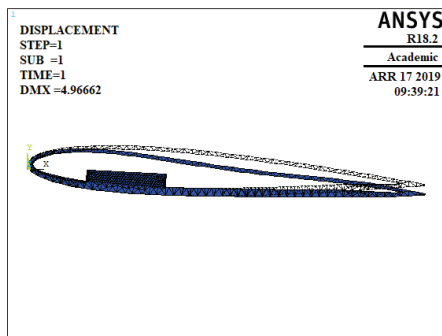


**Figure 7:** Initial shape and deformed shape of the hydrofoil at the first iteration,  $\Delta P = 0.24 \text{ bar}$ ,  $\alpha = 3^\circ$  and  $Re = 0.75 \cdot 10^6$ .

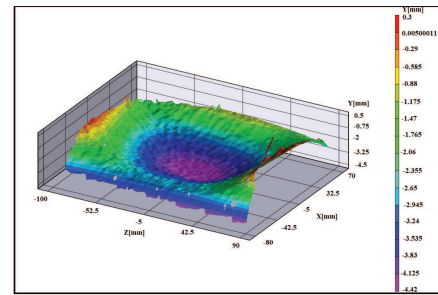
In a first approach, the hydrofoil materials is considered as a homogeneous elastic equivalent. Based on experimental measurements of the displacement for various cavity pressures, the equivalent Young modulus used on the computation was set to  $E = 70000 \text{ MPa}$  and the equivalent Poisson coefficient was set to of 0.34.

Figure 7 presents the initial and deformed shapes of the hydrofoil at  $3^\circ$  angle of attack,  $Re = 0.75 \cdot 10^6$  and an imposed pressure cavity of  $0.24 \text{ bar}$ . The calculated maximum chordwise displacement of the hydrofoil was found to be 3.3 percent of the chord length.

## 5 RESULTS AND DISCUSSION

### 5.1 Hydrofoil deformation and hydrodynamic forces

The effect of cavity pressure on the hydrofoil deformation is investigated by using digital image correlation (DIC-3D). For  $\Delta P = 0.415 \text{ bar}$ , the displacement field as a function of the foil coordinates is presented in figure 8. It is observed that the maximum displacement is  $8.06 \text{ mm}$  (5.3%) located at the center of the hydrofoil. The deformation is not uniform along the spanwise direction due to the structural boundary conditions at the root and the tip.



**Figure 8:** DIC 3D displacement,  $\Delta P = 0.415 \text{ bar}$ .

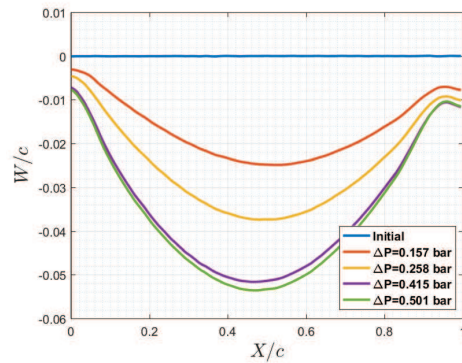


**Figure 9:** Experimental hydrofoil displacement in open air as a function of the chord and the cavity pressure at  $Z/c = 0.55$ .

The displacement of the hydrofoil as function of the chord is extracted at  $Z/c = 0.55$  for four cavity pressures. It is plotted on figure 9. It confirms the results of the 3D displacement field presented in figure 8. The hydrofoil deformations are also measured with a micrometric touch probe at  $X/c = 0.33$  and  $Z/c = 0.63$ . The results are compared to the numerical simulation and the results of the DIC-3D system at the same point (figure 10). As shown in figure 8, the displacement is linear for a cavity pressure up to  $\Delta P = 0.4 \text{ bar}$  and reach a limit value of about  $0.045c$ . The numerical results are in good agreement with experimental ones for a cavity pressure up to  $\Delta P = 0.4 \text{ bar}$ .

showing that the equivalent homogeneous model is fairly consistent with the experiment. Beyond  $\Delta P = 0.4 \text{ bar}$ , the numerical deformation increases linearly exhibiting no saturation.

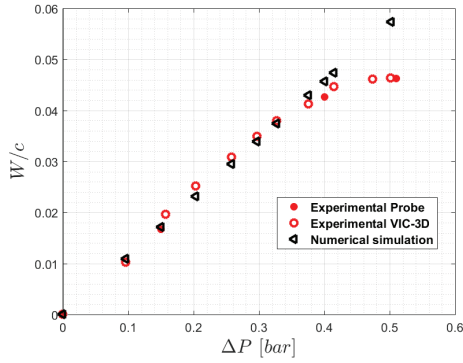


**Figure 10:** Experimental and numerical displacement in open air at  $Z/c = 0.33$  and  $X/c = 0.63$ .

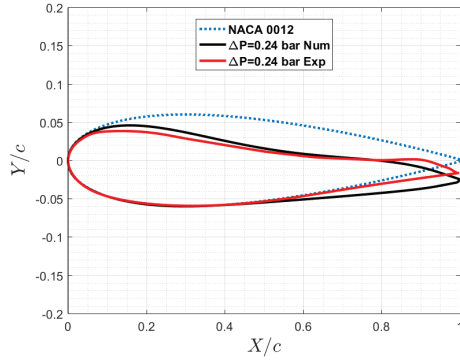
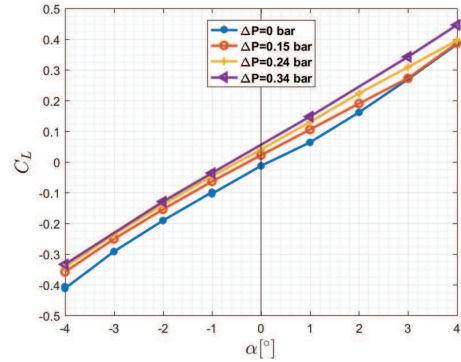


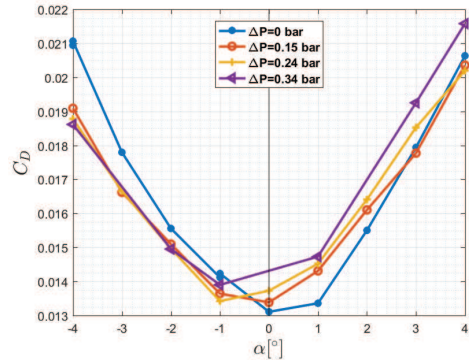
**Figure 11:** Experimental and numerical foil sections,  $\Delta P = 0.24 \text{ bar}$  and  $V = 5 \text{ m/s}$ .

The foil deformation is then analyzed using the scanning measurement system in the hydrodynamic tunnel for a velocity of  $5 \text{ m/s}$ . The experimental deformed section is presented in figure 11 for a cavity pressure  $\Delta P = 0.24 \text{ bar}$  and compared to the numerical one. As depicted in figure 11, the experimental and numerical displacements have the same trend excepted at the trailing edge where a significant difference is observed. This difference is due to the twist of the hydrofoil in the experiment that is not observed with a 2D computation in the numerical study. The connection between the core beam (figure 7) and the low pressure side skin is indeed flexible and allows the all section to rotate around the cantilever one. The hydrodynamic forces for different cavity pressures are presented in figure 12.a and figure 12.b. It is reminded that the pressure inside the cavity decreases then  $\Delta P$  increase. It is shown that the lift coefficient shifts upwards as  $\Delta P$  increases with a slight change in the slope. For the range of angles of attack and cavity pressure of the present experiments, it is found that the lift coefficient increases linearly for both parameters. The results of figure 12.a can be represented by the response surface of the compliant hydrofoil in terms of lift

coefficient versus angle of attack and the non dimensional cavity pressure (figure 13) showing the operating domain of the compliant hydrofoil as a function of the two independent variables.



a. Lift coefficient



b. Drag coefficient

**Figure 12:** Experimental lift and drag coefficients as a function of angle of attack and a cavity pressure at  $Re = 0.75 \cdot 10^6$ .

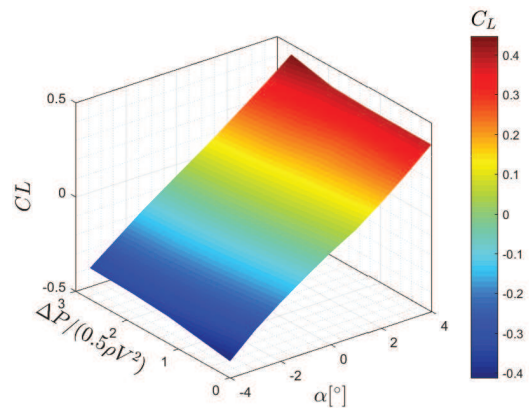


**Figure 13:** Experimental surface response of the lift coefficient as a function of angle of attack and cavity pressure at  $Re = 0.75 \cdot 10^6$ .

If it is considered that the cavity pressure changes the thickness (see figure 10) and the camber linearly, a linear approximation of the response surface (figure 13) can be

given by:

$$C_L(\Delta P^*, \alpha) = 0.109(1 - k(\tau + a\Delta P^*))\alpha + b\Delta P^* \quad (1)$$

Where  $\Delta P^* = \frac{\Delta P}{q}$  is the non dimensional pressure cavity and  $a = 0.013$ ,  $b = 0.025$  and  $k = 0.95$  are constants determined from linear regressions on experimental data constants depending on the material and hydrofoil design.

This simple expression highlights the effect of the pressure on lift slope and lift coefficient described experimentally. The expression of the surface response depending on flow conditions and design parameters can be very useful in the context of foil optimization methods. A same approach could be done regarding the drag coefficient and the lift to drag ratio as well.

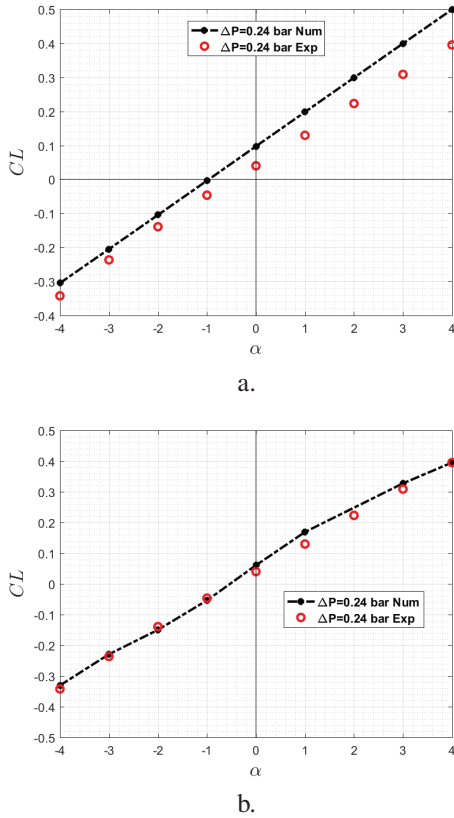


**Figure 14:** Experimental and numerical lift coefficients as a function of the angle of attack for a cavity pressure  $\Delta P = 0.24 \text{ bar}$  and  $Re = 0.75 \cdot 10^6$ . a. Fully FSI computation. b. Flow computation over the experimental deformed sections at mid-span

Figure 14.a shows the experimental and numerical lift coefficient obtain from the FSI algorithm. The numerical lift coefficient is in good agreement with the experimental but departs progressively from the experiment as the angle of attack progressively increases. The reason of the discrepancies can be found in the analysis of the structure.

Indeed, the experimental section shapes and displacements of the compliant wall are extracted at mid-span for  $\alpha$  ranging from  $-4^\circ$  to  $4^\circ$  and they are shown on figure 15 and 16 for positive and negative angle of attack respectively.

A close examination shows that a small flap effect is observed experimentally at the trailing edge affecting the lift coefficient. This effect is not showed by the 2D structural solver where the connection between the skin and the structural beam is considered rigid. Moreover the whole section rotates around  $0.25X/c$  due to a slight twisting of the structural internal beam as previously described. This is particularly observed for positive angle of attack. The foil twisting tends to reduce the angle of attack, therefore to decrease the lift coefficient. It is observed that the FSI computation fits very well the experiments for negative angles of attack when the twist can be neglected. Moreover for positive angles of attack, the twist observed experimentally is not seen into the FSI simulation. This is clearly shown in figure 14.b where the lift coefficient is computed directly on the experimental deformed sections at mid-span. In that case, the numerical lift compares well with the experiments all over the angle of attack range. The parameters should be explored as they can impact the numerical-experimental comparison as structural model, geometry, material properties (isotropic or orthotropic), structural boundary conditions, 3D effects, flow confinement in the test section.

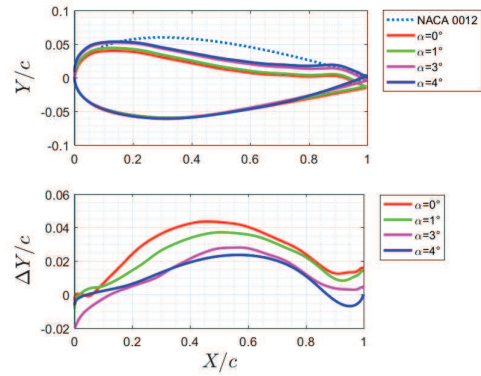


**Figure 15:** Experimental mid-span shapes and associated displacements for  $\Delta P = 0.24 \text{ bar}$ ,  $Re = 0.75 \cdot 10^6$  and  $\alpha = 0^\circ$ ,  $\alpha = 1^\circ$ ,  $\alpha = 3^\circ$  and  $\alpha = 4^\circ$  compared to a NACA 0012.

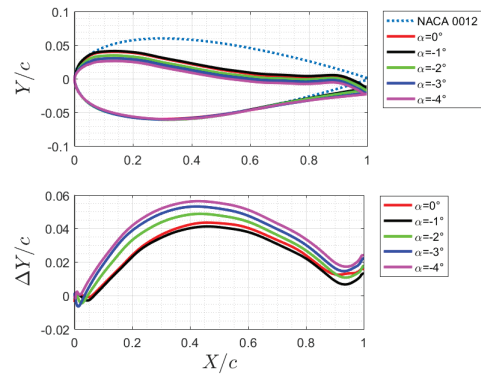


**Figure 16:** Experimental mid-span shapes and associated displacements for  $\Delta P = 0.24 \text{ bar}$ ,  $Re = 0.75 \cdot 10^6$  and  $\alpha = 0^\circ$ ,  $\alpha = -1^\circ$ ,  $\alpha = -2^\circ$ ,  $\alpha = -3^\circ$  and  $\alpha = -4^\circ$  compared to NACA 0012.

## 5.2 Cavitation control

Eventually, the effect of the cavity pressure on the cavitation is briefly analyzed. The effect of the cavity pressure on the theoretical cavitation inception is numerically predicted using the FSI algorithm. Figure 17 shows the lift coefficient versus the opposite of the minimum pressure coefficient ( $-C_{pmin}$ ) for the compliant hydrofoil under different cavity pressure. The cavity pressure has a direct influence on the theoretical cavitation inception, particularly for lift coefficients larger than  $-0.1$ .

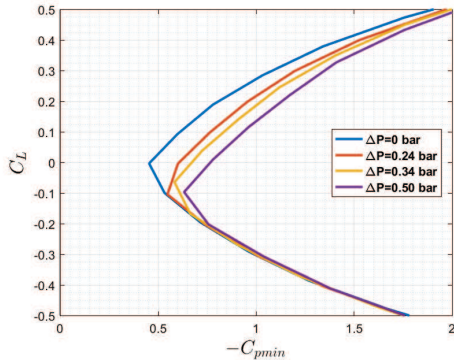


**Figure 17:** Numerical cavitation bucket,  $Re = 0.75 \cdot 10^6$ ,  $\Delta P = 0.24 \text{ bar}$ ,  $\Delta P = 0.34 \text{ bar}$  and  $\Delta P = 0.50 \text{ bar}$ .

Experimentally, the figure 18.a shows the cavitation inception for a cavity pressure equal to  $0.69 \text{ bar}$ , an angle of attack  $\alpha = 7.4^\circ$  and a cavitation parameter  $\sigma = 3.8$  at a Reynolds number of  $10^6$ . For identical conditions, it can be shown that the cavitation disappears (figure 18.b) by decreasing the cavity pressure to  $0.38 \text{ bar}$ . A slight decrease of the lift coefficient from  $0.754$  to  $0.805$ . Figure 19 shows the corresponding hydrofoil shapes at cavitation inception and desinence. The cavitation on compliant structure needs to be more deeply studied. However the first results are encouraging and open the way to control cavitation by compliant hydrofoil.



a. Cavitation inception  
 $C_L = 0.805$   
 $\Delta P = 0.69 \text{ bar}$



b. Cavitation desinence  
 $C_L = 0.754$   
 $\Delta P = 0.38 \text{ bar}$

**Figure 18:** Cavitation inception and desinence on a compliant composite hydrofoil,  $Re = 10^6$ ,  $\alpha = 7.4^\circ$  and  $\sigma = 3.8$ .

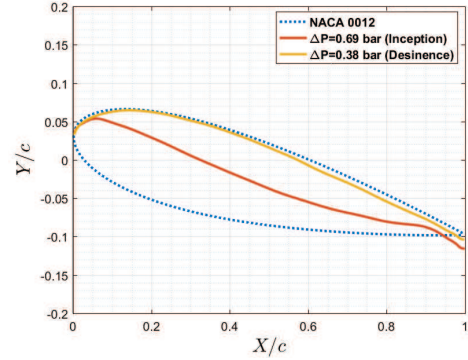


**Figure 19:** Experimental hydrofoil shapes at cavitation inception and desinence at  $Re = 10^6$ ,  $\alpha = 7.4^\circ$  and  $\sigma = 3.8$ .

## 6 CONCLUSIONS

In this paper, an experimental and numerical study is presented in order to assess the effect of the cavity pressure on the hydrodynamic performance of a compliant composite hydrofoil. The compliant hydrofoil is controlled by a cavity driven by pressure (suction). It is tested in a cavitation tunnel at  $Re = 0.75 \cdot 10^6$  at different angles of attack. Firstly, the hydrofoil deformations are measured in open air using digital image correlation (DIC-3D) and a micrometric touch probe. Secondly, experiments are performed in a hydrodynamic tunnel where the lift and drag coefficient are measured using a hydrodynamic balance together with the compliant skin deformation using a scanning laser measurement system.

A 2D numerical fluid structure coupling is developed in accordance with the experiments. It is based on an iterative method coupling the flow solver Xfoil and the structural solver ANSYS-Mechanical. The experiments and the simulations are carried out at different angles of attack and various imposed cavity pressures. The experiments show that cavity low pressure variation has a significant effect on the hydrofoil shape and on the hydrodynamic forces. The cavity low pressure variation conducts to section variations (thickness, camber) together with a slight overall twisting and a small flap effect at the trailing edge. The increase of the suction cavity tends to increase the lift coefficient and to decrease the lift coefficient slope. A response surface depending on both the angle of attack and the cavity pressure can be simply derived linear approximation. It is also showed that for the same angle of attack and the same inflow velocity, it is possible in some extend to suppress the cavitation by changing the cavity pressure. More advanced experimental and numerical studies have to be performed and are in progress. The morphing hydrofoil model developed in this work based on a compliant composite structure driven by a cavity pressure provides encouraging results to control the hydrodynamics forces and the cavitation opening the way to optimization methods to enhance hydrodynamics performance based on Fluid Structure Interactions.

## ACKNOWLEDGMENTS

The authors would like to thank the technical staff of the French Naval Academy Research Institute, as well as Research Institute in Civil Engineering and Mechanics (Saint-Nazaire) for their support to this study.

## REFERENCES

- Brailovski, V., Terriault, P., Coutu, D., Georges, T., Morellon, E., Fischer, C., & Brub, S. (2008). 'Morphing laminar wing with flexible extrados powered by shape memory alloy actuators'. American Society of Mechanical Engineers ASME 2008 Conference on Smart Materials, Adaptive Structures and Intelligent Systems, pp. 615–623.
- Coraddu, A., Oneto, L., Baldi, F., & Anguita, D. (2018). 'Vessels fuel consumption: A data analytics perspective to sustainability'. In Soft Computing for Sustainability Science, Springer, Cham, pp. 11–48.
- De Barros, S., Fadhill, B. M., Alila, F., Diop, J., Reis, J. M L, Casari, P., & Jacquemin, F. (2018). 'Using blister test to predict the failure pressure in bonded composite repaired pipes'. Composite Structures.
- Dimino, I., Lecce, L., & Pecora, R. (2017). Morphing Wing Technologies Large Commercial Aircraft and Civil Helicopters. Butterworth-Heinemann.
- Ducoin, A., Astolfi, J. A., & Sigrist, J. F. (2012). 'An experimental analysis of fluid structure interaction on a flexible hydrofoil in various flow regimes including cavitating flow'. European Journal of Mechanics-B/Fluids **36**(1), pp. 63–74.
- Coraddu, A., Oneto, L., Baldi, F., & Anguita, D. (2018). 'Vessels fuel consumption: A data analytics perspective to sustainability'. In Soft Computing for Sustainability Science, Springer, Cham, pp. 11–48.
- Garg, N., Lyu, Z., Dhert, T., Martins, J., & Young, Y. L. (2015). 'High-fidelity hydrodynamic shape optimization of a 3-d morphing hydrofoil'. In Fourth International Symposium on Marine Propulsors.
- Georges, T., Brailovski, V., Morellon, E., Coutu, D., & Terriault, P. (2009). 'Design of shape memory alloy actuators for morphing laminar wing with flexible extrados'. Journal of Mechanical Design **131**(9), 091006.
- Giovannetti, L. M., Banks, J., Ledri, M., Turnock, S. R., & Boyd, S. W. (2018). 'Toward the development of a hydrofoil tailored to passively reduce its lift response to fluid load'. Ocean Engineering **167**(1), pp. 1–10.
- Lelong, A., Guiffant, P., & Astolfi, J. A. (2018). 'An Experimental Analysis of the Structural Response of Flexible Lightweight Hydrofoils in Cavitating Flow'. Journal of Fluids Engineering **140**(2), 021116.
- Marchand, J. B., Astolfi, J. A., & Bot, P. (2017). 'Discontinuity of lift on a hydrofoil in reversed flow for tidal turbine application'. European Journal of Mechanics-B/Fluids **63**, pp. 90–99.
- Sacher, M., Durand, M., Berrini, E., Hauville, F., Duvi-gneau, R., Le Maitre, O., & Astolfi, J. A. (2018). 'Flexible hydrofoil optimization for the 35th America's Cup with constrained EGO method'. Ocean Engineering **157**, pp. 62–72.
- Weisshaar, T. A. (2013). 'Morphing aircraft systems: historical perspectives and future challenges'. Journal of Aircraft.
- Young, Y. L., Garg, N., Brandner, P. A., Pearce, B. W., Butler, D., Clarke, D., & Phillips, A. W. (2018). 'Load-dependent bend-twist coupling effects on the steady-state hydroelastic response of composite hydrofoils'. Composite Structures **189**, pp. 398–418.
- Zarruk, G. A., Bra,der, P. A., Pearce, B., W & Phillips, A. W. (2014). 'Experimental study of the steady fluid-structure interaction of flexible hydrofoils'. Journal of Fluids and Structures **51**, pp. 326–343.